

# Monolithic polarizing circular dielectric gratings on bulk substrates for improved photon collection from InAs quantum dots

Ryan A. DeCrescent<sup>1,\*</sup>, Zixuan Wang<sup>1,2</sup>, Poolad Imany<sup>1,2</sup>, Sae Woo Nam<sup>1</sup>, Richard P. Mirin<sup>1</sup>, and Kevin L. Silverman<sup>1,†</sup>

<sup>1</sup>*National Institute of Standards and Technology, Boulder, Colorado 80305, USA*

<sup>2</sup>*Department of Physics, University of Colorado, Boulder, Colorado 80309, USA*



(Received 2 October 2023; revised 15 November 2023; accepted 21 November 2023; published 7 December 2023)

III-V semiconductor quantum dots (QDs) are near-ideal and versatile single-photon sources. Because of the capacity for monolithic integration with photonic structures as well as optoelectronic and optomechanical systems, they are proving useful in an increasingly broad application space. Here, we develop monolithic circular dielectric gratings on bulk substrates—as opposed to suspended or wafer-bonded substrates—for greatly improved photon collection from InAs quantum dots. The structures utilize a unique two-tiered distributed-Bragg-reflector structure for vertical electric field confinement over a broad angular range. Opposing “openings” in the cavities induce strongly polarized QD luminescence without harming collection efficiencies. We describe how measured enhancements depend on the choice of collection optics. This is important to consider when evaluating the performance of any photonic structure that concentrates far-field emission intensity. Our cavity designs are useful for integrating QDs with other quantum systems that require bulk substrates, such as surface acoustic wave phonons.

DOI: [10.1103/PhysRevApplied.20.064013](https://doi.org/10.1103/PhysRevApplied.20.064013)

## I. INTRODUCTION

III-V semiconductor quantum dots (QDs) are recognized as quintessential solid-state single-photon sources for quantum photonic technologies [1]. They emit on-demand indistinguishable single photons at gigahertz rates with nearly lifetime-limited spectral line widths [2–4]. Their charge states can be deterministically controlled with simple semiconductor gate structures and their resonance frequencies can be Stark tuned within the same device layout [3,5]. These features—combined with the possibility of monolithic integration—offer tremendous opportunities for interfacing III-V QDs with other two-level systems and for incorporating them into larger hybrid systems and circuits such as optoelectronic or optomechanical systems [6–12].

One universal obstacle for the implementation of QD light sources is due to the relatively large refractive-index mismatch between the host medium (e.g., GaAs) and vacuum. The majority of the photons generated in a bulk material experience total internal reflection at the semiconductor-vacuum interface, ultimately limiting photon-collection efficiencies to  $\lesssim 1\%$  when using vertical collection and external optics. A wide variety of photonic structures have been developed to efficiently

interface with QDs for both on-chip and free-space applications [13]. Some examples include photonic crystal waveguides [14,15], ridge waveguides and ring resonators [16,17], and microdisk resonators [18,19], all of which are particularly useful for on-chip routing of photons to and from QDs. For free-space applications, micropillar cavities [20,21], photonic crystal cavities [22], circular-grating resonators [23–29] and open tunable microcavities based on distributed Bragg reflectors (DBRs) [30] have been demonstrated. Such architectures are often designed to optimize a specific metric, e.g., photon-collection efficiency, strong exciton-photon coupling, optical coherence times, or total brightness. Though this is suitable for pure photonic applications, these structures often cannot be immediately incorporated into larger hybrid structures where the QD needs to interact well with another system.

An example hybrid system that encounters this challenge is a microwave-to-optical transducer based on InAs QDs and surface acoustic wave (SAW) resonators [7,8]. This technology requires optimized electrical, mechanical, and optical structures to be colocated while minimally afflicting the other subsystems. Recent work has shown remarkable success but poor optical collection from the QDs has been a significant source of total end-to-end efficiency losses. Specifically, a bare GaAs surface is ideal for high-quality-factor SAW resonators but leads to poor photon collection from the QD. On the other hand, most previously developed photonic structures for optimal

\*ryan.decrescent@nist.gov

†kevin.silverman@nist.gov

photon collection will strongly scatter the SAW field, reducing mechanical quality factors, or change the mode shape completely. This hybrid system thus requests a photonic structure monolithically incorporated into a bulk substrate while minimally perturbing the SAW strain field. The current work is largely motivated by this goal but our cavity designs may be useful for any application where quantum emitters must be embedded in bulk substrates, such as integrating with bulk acoustic resonators [31] or similar vertical acoustic microcavities [32].

Our designs are based on circular dielectric gratings, or “bullseye cavities,” which have been shown to greatly improve vertical extraction of single photons emitted from InAs and GaAs QDs [23–29] and diamond-vacancy centers [33] and are favorable for their versatility and relatively simple design. Previous work has used suspended membranes [23] or wafer-bonded (“flip chip”) III-V layers [24–27,29] to vertically confine the optical fields so that the emitted photons readily interact with the radial bullseye structure. Here, we show how to achieve effective vertical field confinement by using a unique two-tiered DBR structure. This offers several potential advantages over suspending or wafer-bonding approaches, including even greater ease of fabrication and maintaining larger distances between the QD and etched surfaces. In order to make these structures compatible with SAW resonators, we open the optical cavities on two sides so that focused SAWs can propagate through them with minimal scattering. This opening also creates an optical anisotropy that leads to highly polarized luminescence while negligibly affecting optical performance for the cavity-polarized emission mode. This polarized behavior is compatible with the proposed SAW-based transducer since the optomechanical interaction is not spin dependent. We measure approximately 100 $\times$  photon-collection improvements from QDs in our bullseye cavities when compared to unstructured regions on the same substrates; calculations suggest that this corresponds to approximately 30 $\times$  improvements compared to a traditional DBR structure.

## II. DESIGN AND FABRICATION

Our devices [Fig. 1(a)] consist of a GaAs slab (thickness  $t$ ) above two distinct DBR regions. The lower DBR consists of 22 periods of AlAs/GaAs and is designed to reflect normal-incidence light (“normal DBR”). The upper DBR consists of 2.5 periods of relatively thick AlAs/GaAs layers and is designed to reflect oblique-incidence light at angles around 63° (“oblique DBR”). InAs QDs are grown at the center of the upper GaAs slab. Circular trenches with depth  $d$  are etched into the resulting heterostructure, defining the optical bullseye cavity. The fabricated devices used 20 trenches in total, although numerical calculations suggest that 8–10 trenches are sufficient for good performance. The normal DBR reflects light that would otherwise be

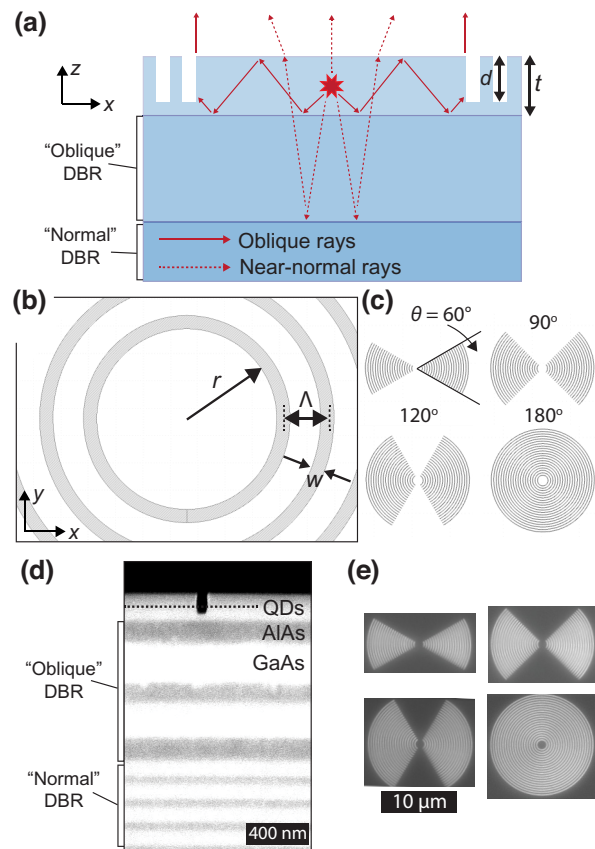


FIG. 1. (a) A cross-section schematic ( $x$ - $z$  plane) of the device. Etched grooves (white regions) and “Normal DBR” (dark blue) and “Oblique DBR” (light blue) regions are designated. The red lines illustrate how light emitted from a QD (red star) at various angles interacts with the structure. (b) The in-plane ( $x$ - $y$ ) structure of the center of the device, illustrated to scale. Gray corresponds to etched regions. Several design parameters are designated in (a) and (b). (c) The full in-plane structures of four devices, illustrated to scale, differing only by a cavity enclosure angle  $\theta$ . (d) A cross-section SEM of the wafer structure: white regions, GaAs; gray regions, AlAs. Distinct normal-DBR and oblique-DBR regions are designated. A single etched groove is apparent. QDs are grown at the center of the top GaAs slab (black dotted line). (e) Plan-view SEM images of four distinct devices, corresponding to the four devices in (c). The 10- $\mu\text{m}$  scale bar applies to (e) and (c).

lost into the bulk substrate but is only effective within an angular range spanning approximately 20° around normal incidence (Appendix A). The upper oblique DBR is intended to emulate a slab waveguide so that light emitted at larger angles (55° to 70°) readily interacts with the circular grating. The basic radial geometry is defined by three parameters [Fig. 1(b)]: the center radius ( $r$ ), the trench periodicity ( $\Delta$ ), and the trench width ( $w$ ). The design parameters are optimized by estimating device performance using commercial finite-difference time-domain

TABLE I. The numerically optimized geometrical parameters.

Parameter	Value
Normal-DBR layer thicknesses	81.0 nm (AlAs) / 69.2 nm (GaAs)
Oblique-DBR layer thicknesses	188.2 nm (AlAs) / 188.2 nm (GaAs)
GaAs slab thickness, $t$	172 nm
Grating etch depth, $d$	$0.83t = 142.7$ nm
Grating periodicity, $\Lambda$	325 nm
Trench width, $w$	$0.21\Lambda = 68$ nm
Cavity center radius, $r$	$2.025\Lambda = 658$ nm

software. We emphasize that although cavity quality factors ( $Q$ ) and Purcell factors are used in initial numerical design optimization, our intended optomechanics applications do not demand high  $Q$  or high Purcell factors; improved photon collection is the primary concern. The final design parameters are specified in Table I and in the text when relevant.

Finally, we symmetrically open the cavity trenches such that opposing etched minor arcs span an angle  $\theta < 180^\circ$ . Three partially enclosed cavities with cavity enclosure angles  $\theta = 60^\circ$ ,  $90^\circ$ , and  $120^\circ$  are illustrated in Fig. 1(c). In this geometry,  $y$ -oriented electric dipoles are expected to interact with the grating while  $x$ -oriented dipoles are expected to be only weakly affected. Fully enclosed cavities with  $\theta = 180^\circ$  are expected to show polarization-independent performance.

Samples are grown via molecular-beam epitaxy and then deposited with a sputtered SiO<sub>2</sub> hard mask. Circular-grating trenches are defined by electron-beam lithography and subsequently etched via reactive-ion etching. The hard mask is then removed by hydrofluoric acid. Figure 1(d) shows a cross-section scanning electron micrograph (SEM) of a fabricated calibration structure; distinct oblique-DBR and normal-DBR regions, as well as a single etched groove, are easily identified. Figure 1(e) shows plan-view SEMs of four cavities with  $\theta = 60^\circ$ ,  $90^\circ$ ,  $120^\circ$ , and  $180^\circ$  [corresponding to structures illustrated in Fig. 1(c)] during an intermediate fabrication step.

The optical bullseye cavities are designed to exhibit an  $(n, l) = (5, 0)$  drumheadlike electromagnetic resonance ( $n$  and  $l$  are the radial and azimuthal quantum numbers of a circular resonator) at 945 nm. This mode choice is somewhat arbitrary; more importantly, the absolute dimensions of the cavity center were chosen to be large enough to accommodate a focused pump beam with minimal scattering from etched regions in future resonance fluorescence measurements (not performed in this work). Numerically calculated electric field magnitude ( $|E|$ ) profiles of this cavity resonance, excited by an  $x$ -oriented electric dipole, are illustrated in Figs. 2(a) and 2(b) for two different plane cuts. These calculations show that the circular-grating

and double-DBR structures generate substantial in-plane [Fig. 2(a)] and out-of-plane [Fig. 2(b)] field confinement. Far-field calculations [Fig. 2(c)] show that a majority of the optical power emitted into the vacuum above the device is contained within an angular range corresponding to a numerical aperture (NA) of 0.25. This directed emission is favorable when long-working-distance collection optics must be used, a scenario commonly encountered with optical cryostats. The cavities also theoretically provide modest Purcell-emission-rate enhancements of approximately 4–5 [Fig. 2(d)]. Here, we use the Purcell spectrum primarily to identify and quantify the cavity resonance. We also quantify the polarizing properties of partially enclosed cavities by comparing the Purcell spectra for  $y$ - and  $x$ -oriented dipoles. These spectra indicate cavity resonances with a typical bandwidth of 10 nm.

For  $y$ -oriented dipoles [Fig. 2(d), top panel], the Purcell enhancement for the  $\theta = 90^\circ$  partially enclosed cavity is reduced by only approximately 25% with respect to the fully enclosed cavity ( $\theta = 180^\circ$ ). In contrast, for  $x$ -oriented dipoles, the Purcell enhancement nearly vanishes for the  $\theta = 90^\circ$  cavity. This is intuitive when considering the radiation patterns for the respective dipole orientations; the  $90^\circ$  enclosed cavity scatters a majority of the radiation field of the  $y$ -oriented dipole but very little of the field of the  $x$ -oriented dipole. In fact, this remains true even for off-center dipoles and polarization-dependent photon-collection enhancements are thus expected to be somewhat robust against QD positioning and to exist regardless of the Purcell effect. Figure 2(e) quantifies these effects by comparing calculated photon-collection rates from our optimized bullseye cavities (“System 1”) to four additional systems [illustrated on the right-hand side and at the bottom of Figure 2(e)]. In all cases, enhancements are defined with respect to a dipole emitting within an unpatterned bulk GaAs substrate. The comparison systems are as follows: “System 2,” a bullseye grating fabricated on a conventional DBR structure comprising a  $1-\lambda$ -thick GaAs on a normal DBR; “System 3,” the same as “System 2” *without* the bullseye grating; “System 4,” our optimized bullseye-cavity geometry *without* the bullseye trenches; and “System 5,” our optimized bullseye geometry *without* the upper oblique DBR. In all cases, collected photons correspond to far-field power contained within an NA of 0.5. Total “rate enhancements” [Fig. 2(e), solid markers] are derived by directly comparing the calculated total far-field power between the test and reference systems. For example, we expect roughly  $100\times$  total rate enhancements from our optimized bullseye gratings (blue; “System 1”) and  $10\times$  total rate enhancements from a conventional  $1-\lambda$  DBR structure (green; “System 3”). Photon “collection enhancements” [Fig. 2(e), open markers]—arising purely from the redistribution of emitted photons due to coherent scattering—are derived by normalizing the far-field power by the respective total radiated dipole

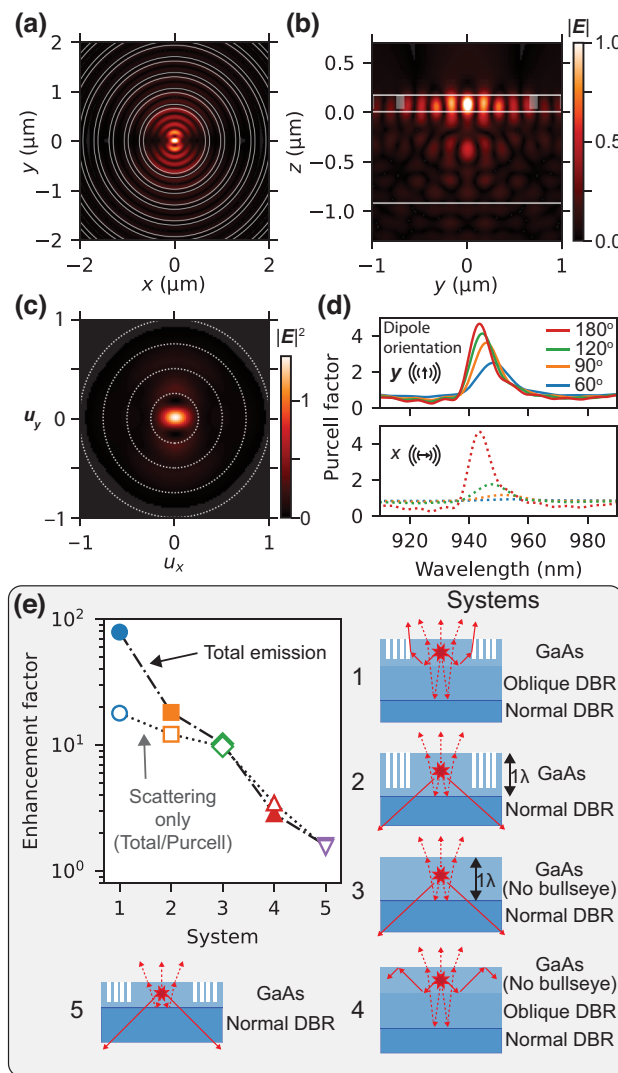


FIG. 2. (a),(b) The calculated electric field magnitude ( $|E|$ ) in (a) the  $x$ - $y$  plane and (b) the  $y$ - $z$  plane when driving a fully enclosed cavity with an  $x$ -oriented electric dipole on resonance at 945 nm. In (a), the edges of the etched regions are designated by white circles. In (b), the boundaries between the DBRs and GaAs slab regions are designated by white horizontal lines and etched regions by gray rectangles. (c) The far-field intensity  $|E|^2$  calculated in vacuum (above the device) under the same conditions as in (a) and (b). The dotted white circles indicate increments of  $NA = 0.25$ . (d) Purcell spectra calculated for  $y$ -oriented (top panel) and  $x$ -oriented (bottom panel, dashed curves) dipoles. The different colors correspond to different cavity enclosure angles  $\theta$  according to the legend. The system geometry (illustrated in each panel) is the same as in Fig. 1(c). (e) Photon-collection enhancements calculated for five different systems (illustrated on the right and below), all with respect to a dipole emitting from within an unpatterned bulk GaAs substrate. “System 1” is our optimized monolithic bullseye grating. “Total rate” includes both Purcell and geometrical enhancements. “Scattering only” excludes changes due to the Purcell factor. (More complete explanations of these terms are provided in the text.) In all cases, the collected photons correspond to power contained in the far field within an  $NA$  of 0.5.

power in each case. For example, a single emitted photon from our device is approximately  $20\times$  more likely to be collected when compared to a bare GaAs surface. Importantly, our optimized structures are still expected to provide  $4\times$ - ( $2\times$ -) higher photon rates (collection) than a conventional  $1-\lambda$  DBR structure even when adding a bullseye grating to that structure (orange; “System 2”). These results indicate that the collection improvement in our system largely originates from the circular gratings and to a lesser extent from the two-tiered DBR structure, although there is a beneficial synergy between these two components.

We can estimate first-lens photon-collection efficiencies for our optimized devices from the numerically calculated collection enhancement. For a single dielectric interface, Snell’s law sets an upper limit on the first-lens collection efficiency. For a single GaAs-air interface, we calculate limits of approximately 0.7% (approximately 2.2%) from an in-plane dipole and  $NA = 0.5$  ( $NA = 1$ ). From these limits and the calculated collection enhancements [Fig. 2(e), blue open marker], we estimate a first-lens collection efficiency of approximately 12.6% for  $NA=0.5$ . This can be compared to approximately 16.6% [29], 23% [25], and 60–80% [28] for wafer-bonded bullseye gratings, approximately 53% for suspended bullseye gratings, or approximately 85% for open tunable DBR microcavities [4]. However, care should be taken when comparing results across the literature, since measured efficiencies depend strongly on the details of the experimental setup [see Fig. 5(a) in Appendix B].

### III. EXPERIMENTAL DEVICE CHARACTERIZATION

For initial experimental characterization, we fabricate the aforementioned devices on wafers grown with a relatively high QD density (approximately ten QDs per  $\mu\text{m}^2$ ). We perform photoluminescence (PL) measurements using a home-built fiber-coupled confocal microscope around an optical cryostat with the sample held at a temperature of approximately 5 K. QDs are optically excited by an 827-nm (nonresonant) pump laser focused to a nearly diffraction-limited spot at the sample surface through an objective with  $NA = 0.7$ . PL is collected by the same objective and then coupled into a single-mode optical fiber. The devices are separated from the collection objective by two optical cryostat windows, which is known to adversely affect mode matching between the collection fiber and the emitted photons and thus decrease end-to-end detection efficiencies. (The importance of the collection geometry is described further in Appendix B.) Reflected pump light is rejected with spectral filters. Polarization-dependent PL spectra are recorded by transmitting the collected PL through a linear polarizer before being coupled into fiber and counted on a CCD spectrometer.

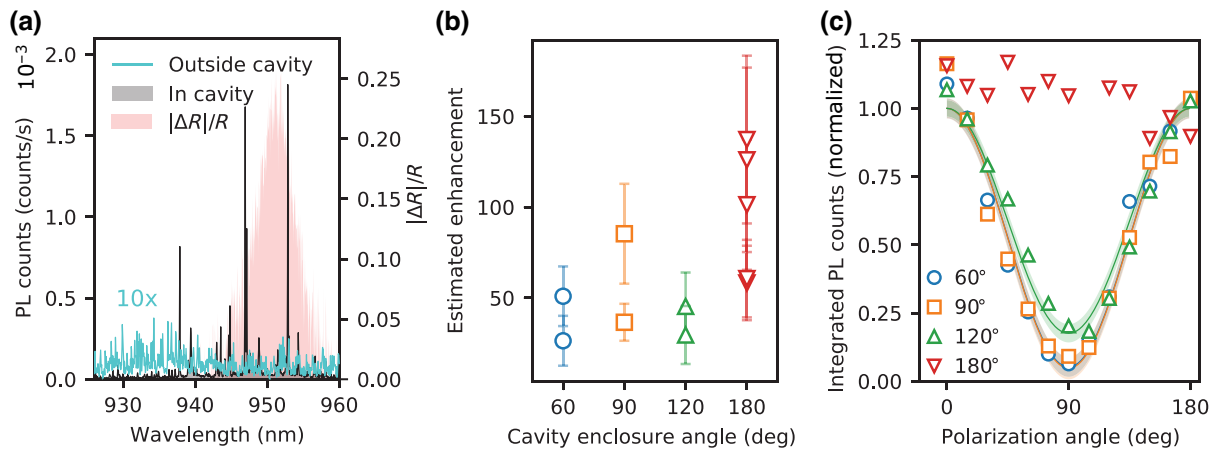


FIG. 3. (a) PL spectra recorded from QDs inside a  $\theta = 90^\circ$  cavity (black) and from a bare region immediately outside the same cavity (light blue; multiplied by 10). The differential reflection spectrum  $|\Delta R|/R$  (red-filled region; right axis) from the same  $\theta = 90^\circ$  cavity is also shown. (b) The estimated collection enhancement for a variety of cavities with different cavity enclosure angles  $\theta$  (horizontal axis). All spectra in (a) and (b) were recorded with  $y$  polarization. Enhancements are calculated by comparing the peak PL counts from a QD inside each cavity to characteristic peak PL counts from QDs immediately outside the cavity. The error bars represent uncertainties arising from the random brightness of each QD in the ensemble; specifically, they were derived by taking ten distinct estimates for the QD count rates outside the cavity within a 10-nm spectral range of the peak PL of the cavity. (c) Experimental PL counts (open markers) of single QD emission lines as a function of the collection polarization angle  $\phi$  for cavities with different enclosure angles  $\theta$  (specified in the legend). (One device of each  $\theta$  was measured and plotted.) Fits to a sinusoidal angular variation are shown by solid curves. Data for  $\theta = 60^\circ$ ,  $90^\circ$ , and  $120^\circ$  cavities are normalized to the fit value at polarization angle  $\phi = 0^\circ$ ; data for the  $\theta = 180^\circ$  cavity is normalized independently.

Typical PL spectra are shown in Fig. 3(a), recorded from inside a partially enclosed cavity ( $\theta = 90^\circ$ , black-filled spectrum) and from an unetched region immediately outside the cavity (light blue, multiplied by 10). Spectra were recorded under identical pump and collection conditions and correspond to  $y$ -polarized emission. At this QD density, approximately 10–15 QDs contribute to each recorded spectrum, yielding approximately 30–45 PL peaks spanning a wavelength range between 920 nm and 960 nm. (Each QD contributes 2–3 PL lines to each spectrum, originating from different charge states and exciton complexes.) Spectra recorded from inside the cavity show only a few (approximately 3–6) intense PL lines with count rates approximately  $20 \times$ – $50 \times$  higher than typical peak values recorded from bare regions. That is, the cavities allow spectral isolation and improved collection of just 2–3 QDs, likely those located near the center of the cavity. The enhanced peaks tend to lie within a 10-nm range around the cavity resonance, as verified by measuring the reflection spectrum of each cavity [e.g., Fig. 3(a), red-filled region]. This indicates that the improved collection indeed originates from a coherent scattering process associated with the designed cavity mode rather than random scattering from etched surfaces. The improved count rate agrees well with the expected enhancements illustrated in Fig. 2(e). Although the dense QD ensemble facilitates cavity characterization, it obscures

decay enhancements predicted from an increased Purcell factor. The emission around 950 nm likely originates from excited states or exciton complexes in our dense QD ensemble, whereas ground-state exciton emission is expected to lie around 1020 nm. Indeed, time-resolved PL measurements did not show obvious acceleration of the QD decay, as would be expected from the calculated Purcell enhancement.

We perform a similar comparison on cavities with enclosure angles of  $\theta = 60^\circ$ ,  $90^\circ$ ,  $120^\circ$ , and  $180^\circ$ . Figure 3(b) summarizes the measured collection enhancements obtained from a variety of cavities with various values of  $\Lambda$ ,  $r$ , and  $w$  (not specified) and  $\theta$  (horizontal axis). Due to the random nature of the brightness and position of each QD in the cavities, the estimated enhancement varies widely between cavities and shows no clear correlation with the enclosure angle  $\theta$ . [The error bars in Fig. 3(b) represent variations expected from the random brightness of QDs in the ensemble.] Nonetheless, typical PL enhancements are estimated to be around  $30 \times$ – $50 \times$ , with an upper estimate of approximately  $140 \times$  from several of the fully enclosed cavities. The measured collection enhancements may be larger than the numerical estimates [Fig. 2(e)], because reduced divergence of the emitted photons leads to less distortion of the wave front when transmitting through the cryostat windows, leading to better mode matching with the single-mode collection fiber

(Appendix B). Further, the measured enhancements are expected to be smaller for high-NA collection objectives [Fig. 5(b)].

A remarkable result is that the PL enhancements for partially enclosed cavities are comparable to those of complete circular cavities—differing only by a factor of approximately 2—when collecting *y*-polarized PL. In contrast, *x*-polarized spectra from partially enclosed cavities resemble spectra recorded from unetched regions, indicating that *x*-polarized collected photons weakly interact with the etched structure. The polarization characteristics of the cavities are summarized in Fig. 3(c). In this analysis, photon counts from individual PL lines are evaluated as a function of the polarization angle. For all partially enclosed cavities, the collected PL is a minimum for *x*-polarized collection (polarizer angle 90°) and a maximum for *y*-polarized collection (polarizer angles 0° and 180°). As a result, the polarization contrast for both  $\theta = 60^\circ$  (blue circles) and  $\theta = 90^\circ$  (orange squares) cavities is approximately 20:1. The polarization contrast decreases to approximately 5:1 for the  $\theta = 120^\circ$  (green up triangles) cavity. Fully enclosed cavities (red down triangles) show no systematic polarization dependence; variations across angles likely arise from variations in the photon-collection efficiencies of our apparatus as the polarizer is rotated. We attribute the observed polarization to the cavity design rather than QD displacement from the cavity center [27], since such polarization dependence was not observed in our fully enclosed ( $\theta = 180^\circ$ ) cavities.

#### IV. DISCUSSION AND CONCLUSIONS

We have detailed the design, fabrication, and optical characterization of circular dielectric gratings for improved photon collection from InAs QDs. As opposed to previous work that has used suspended membranes or wafer-bonded III-V layers for effective vertical field confinement over a broad angular range [23,24], we have designed monolithic structures using a unique two-tiered DBR structure. We have experimentally observed up to 140× photon-collection enhancements when compared to unstructured regions on the same substrate. Based on numerical calculations, we thus anticipate approximately 30× better photon-collection rates when compared to optimized conventional DBR structures. These collection enhancements are engineered to be strongly polarization dependent by simply truncating the angular extent of the grating structures around the QD. These anisotropic structures only weakly impact total collection enhancements.

III-V QDs are very sensitive to localized charges within a several-hundred-nanometer vicinity [34]. Consequently, for best performance, QDs should typically be kept away from interfaces where large surface-defect densities are possible. One potential benefit of our monolithic bullseye gratings is that the nearest etched interfaces (namely,

the bullseye trenches) are more than 650 nm away from bullseye-centered QDs. In contrast, low-quality interfaces may be as close as 90 nm in suspended membranes [23] or 150 nm in wafer-bonded structures [24]. Our devices are also immediately compatible with conventional QD electrostatic *p-i-n* gating methods [3,30] and thus are well suited for improving single-photon source efficiencies while retaining the desired low-noise characteristics of optimized III-V QDs.

#### ACKNOWLEDGMENTS

This research was performed while R.D. held an National Research Council Research Associateship award at the National Institute of Standards and Technology (NIST).

#### APPENDIX A: DESIGN LOGIC OF TWO-TIERED DBR

Figure 4 shows calculated angle-dependent reflectance spectra from three distinct DBR structures. The top two images correspond to the lower (“Normal DBR”) and upper (“Oblique DBR”) regions in our fabricated structures, calculated with 20 DBR periods in each structure. The bottom image corresponds to the fabricated compound two-tiered DBR system with only 2.5 periods in the oblique DBR. For these calculations, an *s*-polarized plane wave is incident from a semi-infinite GaAs layer. The vertical white dashed line indicates the design wavelength where high reflectance around both 0° and approximately 63° are desired.

#### APPENDIX B: COMPATIBILITY BETWEEN PHOTONIC STRUCTURES AND COLLECTION OPTICS

Our experimental setup uses a single-mode optical fiber to collect the emission from the QD. The end-to-end collection efficiencies thus depend on the first-lens collection efficiency and on proper fiber coupling. Generally, the optics needed for best performance when measuring emission from a photonic structure differ from those needed without the photonic structure. For this reason, evaluating the performance of certain photonic structures depends on the larger optical setup and care should be taken when comparing results across systems.

To illustrate the effect, consider the simplified setup shown in Fig. 5(a). Photons emitted from a point source (“emitter”) are collected by an objective (“first lens”) with numerical aperture NA and focused to the tip of a single-mode optical fiber using a lens with focal length  $f$ . Two cases are illustrated. (1) Without a photonic structure (red region surrounded by solid red lines), the maximum angular range over which photons are collected is limited by

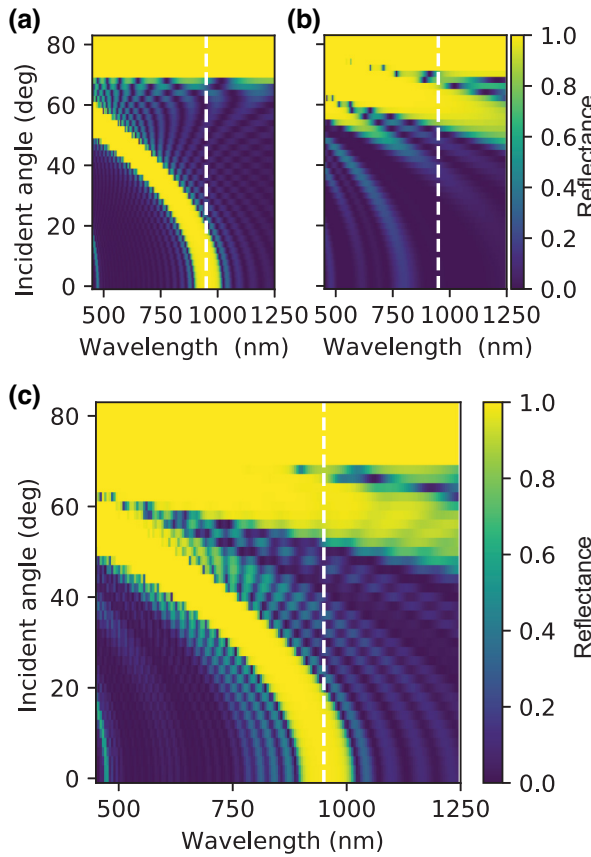


FIG. 4. Calculated angle-dependent reflectance spectra from two distinct DBRs—(a) normal DBR and (b) oblique DBR—and (c) the composite two-tiered DBR used in our fabricated devices.

the objective. At the back aperture, the collimated emission has a beam radius  $r_0$ . A strategic fiber-coupling optic focuses this beam tightly to a diameter  $d_0$  to match the mode field diameter (MFD) of the single-mode collection fiber. (2) With a photonic structure (red region surrounded by dotted red lines), emission is concentrated into a smaller angular range with divergence angle  $\theta_p$ . At the back aperture, the collimated beam thus has a smaller beam radius,  $r_p < r_0$ . The same fiber-coupling optic focuses this beam to a larger diameter,  $d_p > d_0$ , and the fiber coupling suffers.

We first address the impact of the objective. Our experiments (summarized in Fig. 3) used an objective with a nominal NA of 0.7. Two thick optical cryostat windows between the objective and sample perturb the confocal performance of the setup by affecting mode-matching between the collected photons and the single-mode collection fiber. In this case, the bullseye grating that concentrates far-field photons well within NA = 0.25 [e.g., Fig. 2(c)] is tremendously beneficial for fiber coupling; wave-front distortions of the emitted photons are reduced when transmitting through the windows at smaller angles. For objectives with larger NAs housed inside the cryostat, the benefit is expected to be reduced.

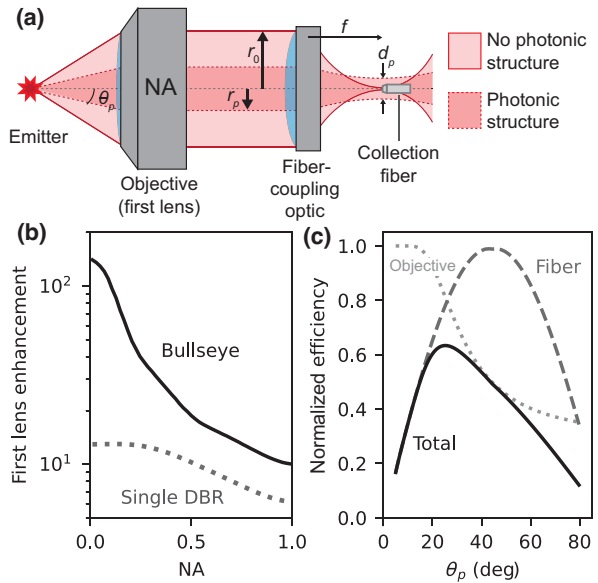


FIG. 5. (a) A schematic setup for collecting emitted photons into a single-mode optical fiber. The fiber-coupling optics were optimized for collection from an emitter without a photonic structure. With a photonic structure, emitted light is concentrated within a cone corresponding to divergence angle  $\theta_p$  (designated by the dotted red contours). The objective collimates this collected light into a beam with radius  $r_p$  and a fiber-coupling lens focuses it to a diameter  $d_p$  that should coincide with the mode field diameter of the fiber for optimal fiber coupling. (b) The numerically calculated first-lens collection enhancement from an optimized bullseye grating as a function of the NA of the objective (black). The enhancement is relative to a bare GaAs substrate. The results for a single conventional DBR are also shown (dotted gray). (c) The collection efficiency for the system as a function of  $\theta_p$  (black). Objective (dotted gray) and fiber-coupling (dashed gray) components are also shown. The objective NA (0.7) and fiber-coupling optics are held constant. The fiber coupling was optimized around 44°, corresponding to NA = 0.7. Each component has been individually normalized to unity.

Figure 5(b) (black solid curve) quantifies how the first-lens collection enhancement depends on the NA of the objective. Here, the calculated far-field intensity from an optimized bullseye grating is normalized to that from a bulk single-interface GaAs geometry, both for the same NA. For  $NA \leq 0.25$ , the first-lens collection enhancements are between 40× and 100×, similar to those observed in our measurements. The values calculated at NA = 1.0 correspond to the ratio of *total* photons emitted into air relative to the substrate. Importantly, the bullseye grating provides approximately 10× better total photon emission into air. For comparison, calculations for a conventional single-DBR geometry (“System 3”) are also shown (gray dotted curve). Bullseye gratings outperform the conventional DBR by at least 2× over all NAs and up to 10× for the smallest NAs.

Figure 5(c) describes semiquantitatively how the end-to-end efficiency varies with the emission divergence angle  $\theta_p$  of the photonic structure. In this example, the fiber-coupling optic was selected to optimize collection for an objective NA = 0.7 ( $\theta = 44^\circ$ ; dashed gray curve). As the photonic structure concentrates light into a divergence angle  $\theta_p$ , the first-lens collection efficiency (dotted gray curve) increases but the fiber-coupling efficiency decreases. The total collection efficiency (solid black curve) is a product of these two efficiencies and reaches a maximum around  $\theta_p = 25^\circ$  (corresponding to NA = 0.24). That is, the *total* collection efficiencies can be further improved by choosing new optimal fiber-coupling optics appropriate for the narrower collected beam radius  $r_p$ .

- [1] P. Senellart, G. Solomon, and A. White, High-performance semiconductor quantum-dot single-photon sources, *Nat. Nanotechnol.* **12**, 1026 (2017).
- [2] L. Monniello, A. Reigue, R. Hostein, A. Lemaitre, A. Martinez, R. Grousson, and V. Voliotis, Indistinguishable single photons generated by a quantum dot under resonant excitation observable without postselection, *Phys. Rev. B* **90**, 041303 (2014).
- [3] M. C. Löbl, I. Söllner, A. Javadi, T. Pregnolato, R. Schott, L. Midolo, A. V. Kuhlmann, S. Stobbe, A. D. Wieck, P. Lodahl, A. Ludwig, and R. J. Warburton, Narrow optical linewidths and spin pumping on charge-tunable close-to-surface self-assembled quantum dots in an ultrathin diode, *Phys. Rev. B* **96**, 165440 (2017).
- [4] N. Tomm, A. Javadi, N. O. Antoniadis, D. Najar, M. C. Löbl, A. R. Korsch, R. Schott, S. R. Valentin, A. D. Wieck, A. Ludwig, and R. J. Warburton, A bright and fast source of coherent single photons, *Nat. Nanotechnol.* **16**, 399 (2021).
- [5] A. Högele, S. Seidl, M. Kroner, K. Karrai, R. J. Warburton, B. D. Gerardot, and P. M. Petroff, Voltage-controlled optics of a quantum dot, *Phys. Rev. Lett.* **93**, 217401 (2004).
- [6] Y. Tsuchimoto, Z. Sun, E. Togan, S. Fält, W. Wegscheider, A. Wallraff, K. Ensslin, A. Imamoglu, and M. Kroner, Large-bandwidth transduction between an optical single quantum dot molecule and a superconducting resonator, *PRX Quantum* **3**, 030336 (2022).
- [7] R. A. DeCrescent, Z. Wang, P. Imany, R. C. Boutelle, C. A. McDonald, T. Autry, J. D. Teufel, S. W. Nam, R. P. Mirin, and K. L. Silverman, Large single-phonon optomechanical coupling between quantum dots and tightly confined surface acoustic waves in the quantum regime, *Phys. Rev. Appl.* **18**, 034067 (2022).
- [8] P. Imany, Z. Wang, R. A. DeCrescent, R. C. Boutelle, C. A. McDonald, T. Autry, S. Berweger, P. Kabos, S. W. Nam, R. P. Mirin, and K. L. Silverman, Quantum phase modulation with acoustic cavities and quantum dots, *Optica* **9**, 501 (2022).
- [9] D. D. Bühler, M. Weiß, A. Crespo-Poveda, E. D. S. Nysten, J. J. Finley, K. Müller, P. V. Santos, M. M. de Lima, and H. J. Krenner, On-chip generation and dynamic

piezo-optomechanical rotation of single photons, *Nat. Commun.* **13**, 6998 (2022).

- [10] C. Papon, Y. Wang, R. Uppu, S. Scholz, A. Wieck, A. Ludwig, P. Lodahl, and L. Midolo, Independent operation of two waveguide-integrated quantum emitters, *Phys. Rev. Appl.* **19**, L061003 (2023).
- [11] M. Finazzer, R. Tanos, Y. Curé, A. Artioli, S. Kotal, J. Bleuse, Y. Genuist, J.-M. Gérard, F. Donatini, and J. Claudon, On-chip electrostatic actuation of a photonic wire antenna embedding quantum dots, *Nano Lett.* **23**, 2203 (2023).
- [12] H. Larocque, M. A. Buyukkaya, C. Errando-Herranz, S. Harper, J. Carolan, C.-M. Lee, C. J. K. Richardson, G. L. Leake, D. J. Coleman, M. L. Fanto, E. Waks, and D. Englund, Tunable quantum emitters on large-scale foundry silicon photonics, *arXiv:2306.06460* [physics, physics:quant-ph] (2023).
- [13] P. Lodahl, S. Mahmoodian, and S. Stobbe, Interfacing single photons and single quantum dots with photonic nanostructures, *Rev. Mod. Phys.* **87**, 347 (2015).
- [14] S. Hughes, L. Ramunno, J. F. Young, and J. E. Sipe, Extrinsic optical scattering loss in photonic crystal waveguides: Role of fabrication disorder and photon group velocity, *Phys. Rev. Lett.* **94**, 033903 (2005).
- [15] T. Lund-Hansen, S. Stobbe, B. Julsgaard, H. Thyrrstrup, T. Sünder, M. Kamp, A. Forchel, and P. Lodahl, Experimental realization of highly efficient broadband coupling of single quantum dots to a photonic crystal waveguide, *Phys. Rev. Lett.* **101**, 113903 (2008).
- [16] I. J. Luxmoore, N. A. Wasley, A. J. Ramsay, A. C. T. Thijssen, R. Oulton, M. Hugues, S. Kasture, V. G. Achanta, A. M. Fox, and M. S. Skolnick, Interfacing spins in an InGaAs quantum dot to a semiconductor waveguide circuit using emitted photons, *Phys. Rev. Lett.* **110**, 037402 (2013).
- [17] L. Dusanowski, D. Köck, E. Shin, S.-H. Kwon, C. Schneider, and S. Höfling, Purcell-enhanced and indistinguishable single-photon generation from quantum dots coupled to on-chip integrated ring resonators, *Nano Lett.* **20**, 6357 (2020).
- [18] P. Michler, A. Kiraz, C. Becher, W. V. Schoenfeld, P. M. Petroff, L. Zhang, E. Hu, and A. Imamoglu, A quantum dot single-photon turnstile device, *Science* **290**, 2282 (2000).
- [19] E. Peter, P. Senellart, D. Martrou, A. Lemaitre, J. Hours, J.-M. Gérard, and J. Bloch, Exciton-photon strong-coupling regime for a single quantum dot embedded in a microcavity, *Phys. Rev. Lett.* **95**, 067401 (2005).
- [20] J. P. Reithmaier, G. Sek, A. Löffler, C. Hofmann, S. Kuhn, S. Reitzenstein, L. V. Keldysh, V. D. Kulakovskii, T. L. Reinecke, and A. Forchel, Strong coupling in a single quantum dot–semiconductor microcavity system, *Nature* **432**, 197 (2004).
- [21] N. Somaschi, V. Giesz, L. De Santis, J. C. Loredo, M. P. Almeida, G. Hornecker, S. L. Portalupi, T. Grange, C. Antón, J. Demory, C. Gómez, I. Sagnes, N. D. Lanzillotti-Kimura, A. Lemaître, A. Auffèves, A. G. White, L. Lanço, and P. Senellart, Near-optimal single-photon sources in the solid state, *Nat. Photon.* **10**, 340 (2016).
- [22] S. Strauf, K. Hennessy, M. T. Rakher, Y.-S. Choi, A. Badolato, L. C. Andreani, E. L. Hu, P. M. Petroff, and

- D. Bouwmeester, Self-tuned quantum dot gain in photonic crystal lasers, *Phys. Rev. Lett.* **96**, 127404 (2006).
- [23] M. Davanço, M. T. Rakher, D. Schuh, A. Badolato, and K. Srinivasan, A circular dielectric grating for vertical extraction of single quantum dot emission, *Appl. Phys. Lett.* **99**, 041102 (2011).
- [24] J. Liu, R. Su, Y. Wei, B. Yao, S. F. C. d. Silva, Y. Yu, J. Iles-Smith, K. Srinivasan, A. Rastelli, J. Li, and X. Wang, A solid-state source of strongly entangled photon pairs with high brightness and indistinguishability, *Nat. Nanotechnol.* **14**, 586 (2019).
- [25] S. Kolatschek, C. Nawrath, S. Bauer, J. Huang, J. Fischer, R. Sittig, M. Jetter, S. L. Portalupi, and P. Michler, Bright Purcell enhanced single-photon source in the telecom O-band based on a quantum dot in a circular Bragg grating, *Nano Lett.* **21**, 7740 (2021).
- [26] H. Singh, D. Farfurnik, Z. Luo, A. S. Bracker, S. G. Carter, and E. Waks, Optical transparency induced by a largely Purcell enhanced quantum dot in a polarization-degenerate cavity, *Nano Lett.* **22**, 7959 (2022).
- [27] T. M. Krieger, C. Weidinger, T. Oberleitner, G. Undeutsch, M. B. Rota, N. Tajik, M. Aigner, Q. Buchinger, C. Schimpf, A. J. Garcia Jr., S. F. C. da Silva, S. Höfling, T. Huber-Loyola, R. Trotta, and A. Rastelli, Post-fabrication tuning of circular Bragg resonators for enhanced emitter-cavity coupling, [arXiv:2309.15801](https://arxiv.org/abs/2309.15801) [physics, physics:quant-ph] (2023).
- [28] Q. Buchinger, S. Betzold, S. Höfling, and T. Huber-Loyola, Optical properties of circular Bragg gratings with labyrinth geometry to enable electrical contacts, *Appl. Phys. Lett.* **122**, 111110 (2023).
- [29] P. Holewa, E. Zieba-Ostój, D. A. Vajner, M. Wasiluk, B. Gaál, A. Sakanas, M. Burakowski, P. Mrowiński, B. Kranjnik, M. Xiong, A. Huck, K. Yvind, N. Gregersen, A. Musial, T. Heindel, M. Syperek, and E. Semenova, Scalable quantum photonic devices emitting indistinguishable photons in the telecom C-band, [arXiv:2304.02515](https://arxiv.org/abs/2304.02515) [physics, physics:quant-ph] (2023).
- [30] D. Najer, I. Söllner, P. Sekatski, V. Dolique, M. C. Löbl, D. Riedel, R. Schott, S. Starosielec, S. R. Valentin, A. D. Wieck, N. Sangouard, A. Ludwig, and R. J. Warburton, A gated quantum dot strongly coupled to an optical microcavity, *Nature* **575**, 622 (2019).
- [31] D. H. Machado, A. Crespo-Poveda, A. S. Kuznetsov, K. Biermann, L. V. Scalvi, and P. V. Santos, Generation and propagation of superhigh-frequency bulk acoustic waves in GaAs, *Phys. Rev. Appl.* **12**, 044013 (2019).
- [32] A. S. Kuznetsov, K. Biermann, A. A. Reynoso, A. Fainstein, and P. V. Santos, Microcavity phonoritons—a coherent optical-to-microwave interface, *Nat. Commun.* **14**, 5470 (2023), Number: 1 Publisher: Nature Publishing Group.
- [33] J. Zheng, A. C. Liapis, E. H. Chen, C. T. Black, and D. Englund, Chirped circular dielectric gratings for near-unity collection efficiency from quantum emitters in bulk diamond, *Opt. Express* **25**, 32420 (2017).
- [34] J. Houel, A. V. Kuhlmann, L. Greuter, F. Xue, M. Poggio, B. D. Gerardot, P. A. Dalgarno, A. Badolato, P. M. Petroff, A. Ludwig, D. Reuter, A. D. Wieck, and R. J. Warburton, Probing single-charge fluctuations at a GaAs/AlAs interface using laser spectroscopy on a nearby InGaAs quantum dot, *Phys. Rev. Lett.* **108**, 107401 (2012).